



Cite this: *Nanoscale*, 2018, **10**, 15103

Activatable magnetic resonance nanosensor as a potential imaging agent for detecting and discriminating thrombosis†

Hang T. Ta,^{id} *^{a,b} Nina Arndt,^{a,d} Yuao Wu,^{a,b} Hui Jean Lim,^a Shea Landeen,^{a,e} Run Zhang,^{id} ^a Danielle Kamato,^b Peter J. Little,^{id} ^b Andrew K. Whittaker^{id} ^{a,c,f} and Zhi Ping Xu^a

The early detection and accurate characterization of life-threatening diseases such as cardiovascular disease and cancer are critical to the design of treatment. Knowing whether or not a thrombus in a blood vessel is new (fresh) or old (constituted) is very important for physicians to decide a treatment protocol. We have designed smart MRI nano-sensors that can detect, sense and report the stage or progression of cardiovascular diseases such as thrombosis. The nanosensors were functionalized with fibrin-binding peptide to specifically target thrombus and were also labelled with fluorescent dye to enable optical imaging. We have demonstrated that our nanosensors were able to switch between the T_1 and T_2 signal depending on thrombus age or the presence or absence of thrombin at the thrombus site. The developed nanosensors appeared to be non-toxic when tested with Chinese Hamster Ovarian cells within the tested concentrations. The working principle demonstrated in this study can be applied to many other diseases such as cancer.

Received 24th June 2018,
Accepted 25th July 2018

DOI: 10.1039/c8nr05095c

rsc.li/nanoscale

1. Introduction

Cardiovascular disease is the leading cause of death worldwide.^{1,2} It is estimated that 795 000 strokes occur each year in the United States; every 40 seconds someone in the United States suffers a stroke and every 4 minutes someone dies.³ Atherosclerotic cardiovascular disease and its life-threatening complication events such as stroke and myocardial infarction are the leading causes of morbidity and mortality, typically due to the formation of thrombi or emboli and subsequent vessel occlusion.⁴ Thrombi are intravascular deposits composed of fibrin and red cells with variable platelet and leukocyte components. The formation of thrombus is activated

when a blood vessel is damaged or an atherosclerotic plaque ruptures. The process involves a range of players including platelets, enzyme thrombin, fibrin and factor XIII.⁵

Imaging is the main approach for identifying thrombus. Currently, thrombus imaging relies on different modalities depending on the vascular bed. Carotid ultrasound is used for carotid thrombus; transesophageal echocardiography (TEE) and contrast-enhanced magnetic imaging (MRI) are for cardiac chamber clots;⁶ Doppler ultrasound is for deep vein thrombosis (DVT);⁷ and computed tomography (CT) is for pulmonary embolism (PE) and stroke detection.^{8–10} Despite some success of these techniques, several thrombotic events and blood clots are not well located and identified until later complications such as pulmonary embolism, stroke and sudden death are observed. In addition, current clinical imaging methods detect thrombus indirectly, relying on anatomical and mechanical vascular abnormalities, or on blood flow deficit, rather than directly imaging the target. Furthermore, none of these modalities provide information on the composition of the thrombus, and none of these is able to detect thrombus from all parts of the body.¹¹

In recent decades, molecular imaging, based on the use of targeted imaging agents to identify specific molecular processes within the disease site such as thrombosis, has attracted a lot of interest as it offers less invasive solution with high sensitivity and specificity, as well as potential whole-body

^aAustralian Institute for Bioengineering and Nanotechnology, the University of Queensland, Brisbane, Queensland, Australia. E-mail: h.ta@uq.edu.au, hangthuta@gmail.com

^bSchool of Pharmacy, the University of Queensland, Brisbane, Queensland, Australia

^cAustralian Research Council Centre of Excellence in Convergent Bio-Nano Science and Technology, Brisbane, Queensland, Australia

^dDepartment of Biotechnology, Technische Universität Berlin, Berlin, Germany

^eDepartment of Biological Engineering, Massachusetts Institute of Technology, Boston, USA

^fCentre of Advanced Imaging, the University of Queensland, Brisbane, Queensland, Australia

† Electronic supplementary information (ESI) available. See DOI: 10.1039/c8nr05095c

applications.^{12,13} MRI is a powerful and indispensable tool in medical research, clinical diagnosis, and patient care. Compared to other modalities, molecular MRI has great potential for thrombus imaging.¹⁴ Iron oxide and gadolinium are two robust contrast agents used in MRI. Iron oxide nanoparticles are T_2 - or T_2^* -weighted MRI agents and provide negative image contrast. They can be detected at a relative low concentration and at a sub-millimeter area.¹⁵ Iron oxide nanoparticles have been widely studied for molecular imaging of thrombosis by targeting its specific biomarkers such as activated platelets.^{14,16–21} Gadolinium (Gd)-based materials are T_1 -weighted MRI agents and provide positive image contrast. The T_1 effect or bright spot imaging is preferred since the location of the imaging agent is more readily distinguishable from potential artefacts produced by tissue interfaces, hemorrhage or signal cancellations at water-fat interfaces, which all produce negative contrast effects.²² T_1 -Weighted imaging is particularly advantageous in imaging of vessel plaque or thrombosis, as a sufficient T_1 shortening effect allows generation of positive contrast between a plaque/thrombus (appearing bright in the image) and surrounding tissues and blood (dark).^{14,23,24} Since both T_1 and T_2 contrast agents have their respective advantages and disadvantages, a targeted dual-contrast iron oxide nanoparticle has been developed recently to take advantages of both T_1 and T_2 contrast effects for imaging of thrombosis.¹⁴

Thrombolytic drugs are used to dissolve blood clots and are used in patients with myocardial infarction, thrombotic stroke, and pulmonary embolism. There are three major classes of thrombolytic or fibrinolytic drugs: tissue plasminogen activator (tPA), streptokinase (SK), and urokinase (UK), with tPA being the most commonly used.²⁵ Hemorrhage or bleeding is the most common side effect of these drugs and it can be life-threatening.²⁶ The success rate of fibrinolytic therapy is higher in fresh thrombosis than in old thrombosis.²⁷ Complete or partial resolution of the thrombotic occlusion was obtained in 94%, 82%, and 69%, respectively, in those patients who presented within 3 days, 1 to 2 weeks, and 3 to 4 weeks after the first appearance of symptom. With a delay of 5 to 8 weeks, the results were uniformly poor with only 1 partial recanalization in 7 patients.²⁷ In another report, in the fresh thrombus group, 17 of 18 thrombi had disappeared; while in contrast, 14 of the 15 old thrombi (age: 4–26 months) remained unchanged in size and deformation.²⁸ Fibrinolytic therapy for old thrombus is not efficient and may put patients at risk of systemic bleeding. Balancing between favourable outcomes and unfavourable side effects is important in guiding thrombolytic treatment. It is critical to not only localize the thrombus but also determine its age to decide accurate treatment regime. Non-invasive differentiation between old and fresh thrombi would be of clinical importance to estimate the risk for embolization and the necessity of thrombolysis.

Although there are a number of MRI methods for imaging of thrombus, all of which have weakness in their approach and there has been no single imaging agent that can simultaneously detect and grade the age of the thrombus. By target-

ing fibrin,^{29–32} both new and aged thrombi can be imaged but these thrombi cannot be distinguished. By targeting the enzymes upregulated in the clotting cascade (e.g. thrombin),³³ it may be possible to visualize fresh thrombus, but aged thrombus cannot be detected. Here we developed a smart MRI nano-sensor that can image and distinguish between fresh and old thrombi. This is a superior approach where a single imaging agent can be used to identify and classify thrombus throughout the body, aiding in the decision process in relation to the likely value and the efficacy of the treatment of patients with thrombolytic therapy.

In this study, a MRI T_1/T_2 switchable nanosensor (iron oxide nanoparticle coated with a detachable layer of Gd) targeting fibrin has been developed to provide a means for non-invasive detection as well as characterization of the disease progression (Fig. 1). The nanosensor exhibited T_2 effect in the absence of thrombin (dark signal) while it showed T_1 effect in the presence of thrombin (bright signal). Such a nanosensor can simultaneously locate a thrombus and provide information on its age since it is capable to switch between T_1 and T_2 signals depending on the age of the thrombus.

This design is based on the fact that in the case of direct contact between T_1 and T_2 agents (gadolinium and iron oxide, respectively), the magnetic field generated by a superparamagnetic T_2 material perturbs the relaxation process of the paramagnetic T_1 material and results in the quenching of the T_1 signal.³⁴ Therefore, we hypothesized that the intact nanosensor would have T_2 signal. If gadolinium is released, its T_1 signal will be restored. As mentioned previously, fibrin is present in both new and old thrombi, this nano-probe can bind to both fresh and constituted thrombi. However, if it binds to an active forming thrombus, thrombin (only active on fresh thrombus) will cleave the linkers between gadolinium and iron oxide core. Iron oxide core will then be washed away,

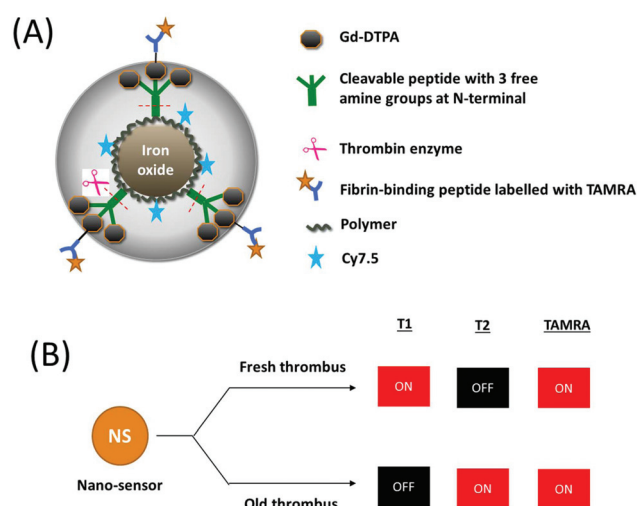


Fig. 1 Design of the MRI T_1/T_2 switchable nanosensor (A) and its working principle (B). The grey hollow sphere represents the layer of Gd-DTPA attached on the nanoparticle. Each cleavable peptide may carry a maximum of three Gd-DTPA.

releasing gadolinium bound on thrombus surface, which then provides T_1 signal. In the case of aged thrombus, because the nanosensor is intact, T_2 signal will be achieved.

The thrombolytic drugs discussed above dissolve blood clots by activating plasminogen, which forms a cleaved product called plasmin. Plasmin, a proteolytic enzyme, is capable of breaking cross-link between fibrin molecules that provide the structural integrity of blood clots. As discussed above, it has been reported that the efficacy of thrombolytic drugs depends on the age of the clots. Old clots have more fibrin cross-linking and are more compact, and therefore are more difficult to dissolve. Thrombin is a serine protease and is produced in large amounts in the blood coagulation cascade.³⁵ Thrombin converts fibrinogen to fibrin, that is, a biological and mechanical sealant for the platelet aggregation. Thrombin also activates coagulation factor XIII (FXIIIa) that cross-links fibrins. Thrombin is present in the beginning of the thrombus formation and is associated with early or new thrombosis. MR imaging of thrombin has been reported, in which the contrast agent is designed based on the assembly of the aptamer functionalized iron oxide nanoparticles in the presence of thrombin.³³ In our study, we used thrombin as a target to distinguish fresh and old thrombus; and synthesized and characterized the thrombin-activatable nanosensors as described above.

2. Materials and methods

All reagents and solvents were obtained from standard commercial sources and were used as received. Peptides (Fig. S1 and S2†) and control peptides were purchased from GeneScript USA Inc.

2.1 Synthesis of iron oxide nanoclusters (IONCs)³⁶

MiliQ-water (15 mL) in a 50 mL round-bottom flask was purged with nitrogen to remove oxygen, followed by the addition of concentrated ammonia solution (1.8 mL, 30%). $\text{FeCl}_3 \cdot 6\text{H}_2\text{O}$ (0.61 g) and $(\text{NH}_4)_2\text{Fe}(\text{SO}_4)_2 \cdot 6\text{H}_2\text{O}$ (0.628 g) were dissolved in 2 mL of diluted HCl (100 μL of 12N HCl in 2 mL miliQ-water).³⁶ The mixture of iron precursors was de-gassed and quickly injected into alkaline solution and the solution was stirred for 10 s at room temperature. 0.8 g of poly(acrylic acid) (PAA) was dissolved in 5 mL of miliQ-water and added into the previous mixture under stirring. After 1 h, the resultant solution was collected and washed by 3 cycles of centrifugation at 14 000 rpm, 30 min and resuspension of nanoparticle pellet with water. The nanoparticles were then store in miliQ-water. No obvious precipitation was observed after several weeks.

2.2 Synthesis of nanosensor

IONCs (1 mg) was resuspended in a 100 μL mixture of phosphate buffered saline (PBS) and dimethyl sulfoxide (DMSO) (volume ratio of 2:8). 2.5 μmoles of *N*-(3-dimethylaminopropyl)-*N'*-ethylcarbodiimide hydrochloride (EDC,

Sigma-Aldrich) and 10.05 μmoles of *N*-hydroxysuccinimide (NHS, Sigma-Aldrich) were dissolved in 40 μL DMSO and added to the IONC solution. The mixture was incubated for 15 minutes with shaking. 156 nmoles of *N*-(2-aminoethyl) maleimide trifluoroacetate (AEM, Sigma-Aldrich) was then added and incubated for 8 hours at room temperature with shaking. The mixture was named mixture A. Mixture B was prepared as follows. 470 nmoles of diethylenetriaminepentaacetic acid gadolinium(III) dihydrogen (Gd-DTPA, Sigma-Aldrich) was incubated with 3.76 μmoles of EDC and 15.08 μmoles of NHS for 15 minutes with shaking. 78.2 nmoles ThrPep (KKLVPRGSL, thrombin-cleavable peptide, Fig. S1†) was dissolved in 50 μL of DMSO and added slowly into the above Gd-DTPA/EDC/NHS mixture and incubated for 8 hours under shaking at room temperature. 312 nmoles of Tris(2-carboxyethyl)phosphine hydrochloride (TCEP-HCl) in 10 μL DMSO was then added to the above solution and incubated for 30 minutes. The final mixture (mixture B) was mixed with mixture A above and incubated overnight at room temperature under shaking. The nanoparticles were then washed by 3 cycles of centrifugation at 14 000 rpm for 20 min and resuspension of nanoparticle pellet with 50 mM NaHCO_3 (pH 8) containing 0.01% Tween-20; and finally redispersed in 10 μL the NaHCO_3 buffer above. After the last centrifugation, T_1 and T_2 of the supernatant were measured and compared with those of buffer solution to ensure there was no free Gd-DTPA. Otherwise, further washing steps would be performed. Fig. S3A† illustrates the conjugations steps to prepare the nanosensor. The control non-activatable nanosensors were prepared similarly but ThrPep was replaced by the non-cleavable d-ThrPep (kklvprgslc).

2.3 Functionalization of the nanosensor with targeting peptide

To functionalize the nanoparticles with fibrin-binding peptide, the nanoparticles were incubated with 9.4 μmoles of EDC and 37.6 μmoles of NHS for 30 minutes (mixture A). 76 nmoles of FibPep (GPRPPGGS[Lys(TMR)]GC, fibrin binding peptide, Fig. S2†) was incubated with 294 nmoles of TCEP-HCl for 30 minutes, followed by the addition of 156 nmoles of AEM. The mixture (B) was incubated for 8 hours at room temperature under shaking. The above nanoparticle solution A was then mixed with the pre-incubated mixture B and incubated overnight at room temperature under shaking. The particles were washed by 3 cycles of centrifugation at 14 000 rpm for 20 min and resuspension of the nanoparticle pellet with 50 mM NaHCO_3 (pH 8) containing 0.01% Tween-20; and finally stored at 4 °C. After the last centrifugation, the supernatant was checked for fluorescence intensity to ensure there was no free peptide left. Otherwise, further washing cycles were performed. These conjugation steps were illustrated in Fig. S3B.† Non-targeting nanosensors were prepared using the same approach but FibPep was replaced with the non-binding peptide ConFibPep (GPSPPGGS[Lys(TMR)]GC). The FibPep and ConFibPep were labelled with pH-insensitive orange-red fluorescence molecule 5-TAMRA (TMR, 5-carboxytetramethyl-

rhodamine) with approximate excitation/emission maxima at 546/579 nm with good photostability. These labelled peptides were provided by GeneScript USA Inc.

2.4 Characterization of the nanoparticles

The hydrodynamic size and zeta potential of the nanoparticles were determined with a Zetasizer nano series (Malvern) equipped with a 4.0 mW He–Ne laser operating at 633 nm and a detection angle of 173°. At least three measurements at 25 °C were made for each sample with an equilibrium time of 2 min before starting measurement. Transmission electron microscope (TEM) images were collected on a Hitachi HT7700 TEM operating at an accelerating voltage of 120 kV. UV-Vis absorbance spectra were obtained *via* a Shimadzu UV-2600 Spectrophotometer. Fluorescence intensity was measured using a Tecan X200 microplate reader. The contents of iron (Fe) and gadolinium (Gd) in the nanoprobe were determined by Inductively Coupled Plasma Optical Emission Spectrometry (ICP-OES). Samples were prepared in 2% HNO₃ for ICP-OES. Peptide concentration was measured by using LavaPep™ Peptide and Protein Quantification Kit (Gel Company, USA) according to manufacturer's instructions.

2.5 Fluorescence imaging

The fluorescence images of the nanosensor solutions and the clots were collected using a Carestream FX-Pro (Bruker Corporation) with a spectral protocol utilizing excitation filter at 540 nm with collection through an 600 nm emission filter set (f-stop 2.80, 2 × 2 binning, 120 mm FOV, 2 s exposure time). To provide location of the clots, fluorescence images were co-registered with a reflectance image (f-stop 2.80, reflectance filter, 120 mm FOV, 0.2 s exposure time). All images were batch exported as 16-bit TIFF images and image processing was completed by Image-J (National Institute of Health, USA).

2.6 NMR T_1 and T_2 measurements

T_1 and T_2 relaxation time measurements were performed at 298 K using Inversion Recovery and Carr–Purcell–Meiboom–Gill (CPMG) pulse sequences, respectively, on a Bruker Ascend 400 NMR spectrometer. Buffered water solutions of the nanosensors were placed in Wilmad coaxial insert tubes with reference capacity of 40 μL and the tubes were inserted into NMR tubes containing D₂O. Data were analysed with TopSpin to obtain T_1 and T_2 relaxation times.

Relaxivities (r_1 and r_2) are generally defined as the slope of the linear regression generated from a plot of the measured relaxation rate ($1/T_i$, where $i = 1, 2$) *versus* the concentration of the contrast agent (iron, Fe):

$$\frac{1}{T_i} = \frac{1}{T_{i(\text{blank})}} + r_i \cdot [\text{Fe}]$$

or

$$R_i = \frac{1}{T_{i(\text{blank})}} + r_i \cdot [\text{Fe}]$$

$$\frac{1}{T_i} - \frac{1}{T_{i(\text{blank})}} = r_i \cdot [\text{Fe}]$$

T_i denotes the longitudinal and transverse relaxation times, T_1 and T_2 , respectively, R_i is relaxation rate, and $T_{i(\text{blank})}$ is the relaxation times of the solvent without nanoparticles.

2.7 Magnetic resonance imaging of nanosensor samples

Magnetic resonance imaging (MRI) of nanosensor solutions was performed on a 9.4 Tesla scanner (Bruker). The parameters used for T_1 -weighted imaging were: echo time (TE) = 3.8 ms; repetition time (TR) = 500 ms; matrix size = 256 × 256; field of view (FOV) = 4 × 4 cm² and slice thickness = 1 mm. The T_2 -weighted imaging was performed using MSME method under the same conditions except of longer TE (7 ms) and TR (2000 ms).

2.8 Degradation and cleavage study

Degradation and cleavage profiles were obtained *via* method adopted from Gunawan *et al.*³⁷ Magnetic relaxation measurement of the nanosensor was conducted with a 400 MHz NMR spectroscopy as described previously in the presence and absence of enzyme thrombin to evaluate the T_1/T_2 switchable capacity. Briefly, samples containing 0.5 mg nanosensors were incubated with thrombin enzyme at different concentrations (0, 0.1, 1 and 2 U mL⁻¹) in 50 μL reaction buffer (50 mM NaHCO₃, pH 8.0) at 37 °C under constant shaking with different incubation periods (up to 24 h). Samples were then prepared in the same buffer for T_1 and T_2 measurements.

2.9 *In vitro* human thrombus binding study

Human fresh frozen plasma (FFP), provided by Australian Red Cross Blood Service, was used to prepare *in vitro* human thrombi. Briefly, 100 μL of FFP was mixed with 5 μL of 0.4 M CaCl₂ and 3 μL of 0.1 U μL⁻¹ thrombin enzyme in a 0.6 mL eppendorf tube. The mixture was incubated at 37 °C for either 12 hours or 7 days to make “fresh” thrombus or “aged” thrombus, respectively. Thrombus was then washed with Phosphate Buffered Saline (PBS) and the nanosensor solution was added on top of the thrombus with or without thrombin enzyme (0.1 U). The mixture was incubated at 37 °C for 4 h with gentle shaking. Finally, the thrombus was washed 3 times with PBS and fixed with 4% paraformaldehyde (PFA). Fluorescence images of the thrombus were taken with a Carestream FX-Pro (Bruker Corporation) as described above.

After fluorescence imaging, 2% low melting point agarose (Sigma) was administered on top of the thrombi. Magnetic resonance imaging (MRI) of agarose-embedded clots was performed on a 9.4 Tesla scanner (Bruker). The embedded-clots were placed within a MRI coil, having the longitudinal axes of the cone-shaped clots oriented horizontally. The parameters used for T_1 -weighted imaging were performed using MSME method with echo time (TE) = 3.8 ms; repetition time (TR) = 500 ms; matrix size = 256 × 256; field of view (FOV) = 4 × 4 cm² and slice thickness = 1 mm. The T_2 -weighted imaging was per-

formed using MSME method under the same conditions except of longer TE (60 ms) and TR (2000 ms).

2.10 Cell culture

All cell culture reagents were obtained from GIBCO/Invitrogen (Australia) unless otherwise noted. Chinese Hamster Ovarian (CHO) cell line attained from the American Type Culture Collection (ATCC). Cells were cultured in Dulbecco's modified Eagle's medium (DMEM) supplemented with 10% fetal bovine serum (FBS), 1% nonessential amino acids (NEAA), and 1% penicillin/streptomycin (P/S) in a humidified 5% CO₂ atmosphere. A seeding cell population of exponentially-growing cells greater than 95% viability was used for all assays.

2.11 Cytotoxicity study

CHO cells were seeded into 96-well plate at a density of 10 000 cells per well. After 24 h incubation, the cells were treated with different concentrations of the nanosensor (0, 0.05, 0.1, 0.2, 0.5, 1, 1.5, 2 mg mL⁻¹; equivalent to 0–0.48 mg Fe per mL and 0–3.1 μg Gd per mL) for 24 hours and 48 hours in a humidified 5% CO₂ atmosphere at 37 °C. After nanoparticle treatment, the proliferation and viability of the cells were evaluated using PrestoBlue™ Cell Viability Reagent (ThermoFisher Scientific) according to manufacturer's protocol. The fluorescence intensity of the cells was measured with a microplate reader Tecan X200 with an excitation wavelength of 560 nm and an emission wavelength of 590 nm.

2.12 Statistical analysis of data

Data are presented as mean ± standard deviation (SD). The graphs were plotted by SigmaPlot® version 13.

3. Results and discussion

3.1 Characteristics of the nanosensors

The nanosensor comprises a core of PAA-coated iron oxide nanocluster (IONC) and an outer layer of gadolinium chelator (Gd-DTPA) on its surface that is connected to the core *via* short thrombin-cleavable peptide linkers (KKLVPRGSLC, named ThrPep) (Fig. S1†). The 10-mer peptide was designed to consist of a thrombin recognition site (LVPRGS), a cysteine amino acid at C-terminus, and two lysine amino acids at N-terminus. Thrombin recognizes the consensus sequence LVPRGS and cleaves the peptide bond between R and G.³⁸ Cysteine (C) is added to introduce free thiol group for conjugation with the IONCs. Double lysine amino acids (K) were added to introduce 3 free amine groups for conjugation with Gd-DTPA. It was expected that one peptide would carry a maximum of three Gd-DTPA groups. A D-amino acid version of ThrPep peptide was synthesized and used as control peptide, and named as d-ThrPep (kklvprgslc). d-ThrPep is not recognized by catalytic thrombin and therefore is non-cleavable. A peptide that binds specifically to fibrin, a major component of thrombus,^{39–41} was also designed and chemically attached to the outer layer of the nanosensor for targeting purpose. The peptide, named

FibPep, comprises 11 amino acids GPRPPGGS[Lys(TMR)]GC and is labelled with TAMRA fluorescence molecule at lysine site to enable optical imaging of the nanosensor (Fig. S2†). A non-binding peptide GPSPPGGS[Lys(TMR)]GC, named ConFibPep, was also designed and served as the control peptide.

ThrPep and d-ThrPep were introduced to carboxylic-IONCs *via* 3 chemical conjugation steps as outlined in Fig. S3A.† FibPep and ConFibPep were added onto the nanosensors *via* 2 ligation steps as outlined in Fig. S3B.† Using Dynamic Light Scattering (DLS), it was found that the bare IONCs (IONCs with only PAA coating) had an average hydrodynamic diameter of 103.2 ± 2.1 nm and a zeta potential of -44.5 ± 1.4 mV while the targeted nanosensor (IONC-ThrPep-GdDTPA-FibPep) constructs had a hydrodynamic diameter of 170.0 ± 1.9 nm and a zeta potential of -29.1 ± 0.7 (Fig. S4A†). TEM image showed that the nanosensors had the size ranging from 20 to 50 nm (Fig. S4B†). The targeted nanosensors (IONC-ThrPep-GdDTPA-FibPep) appeared brown in aqueous solution (Fig. S4C†) and exhibited strong red fluorescence as FibPep was labelled with TAMRA (Fig. S4D†). UV-Vis absorbance spectra of the nanosensor, FibPep and FibPep-nanosensor are shown in Fig. S4E† and confirmed the successful attachment of FibPep to the nanosensors.

3.2 Dependence of magnetic relaxation activation on peptide grafting density

Since grafting density of peptide (the number of peptide molecules) on the iron oxide nanoparticle's surface might affect the accessibility of thrombin to the cleavage site, grafting density was varied and investigated to determine an optimum value. Degradation or cleavage profiles were obtained *via* a method adopted from Gunawan *et al.*³⁷ Magnetic relaxation measurements of the nanosensor were conducted with a 400 MHz NMR instrument in the presence or absence of thrombin to evaluate the T_1/T_2 switchable capacity. Different nanosensors (IONC-ThrPep-GdDTPA) were prepared with different peptide grafting densities, varying from 20 to 67 nmoles mg⁻¹ nanoparticles (6.9 × 10⁻¹²–23.1 × 10⁻¹² nmoles of peptide per nanoparticle or 0.13–0.44 peptide per nm² of nanoparticle surface area). They were named NS1, NS2, NS3 and NS4, respectively. The nanosensors were exposed to simulated thrombotic conditions (50 × 10⁻³ M NaHCO₃, pH 8)³⁷ without or with thrombin at a concentration of 1 unit per mL.

T_1 (spin-lattice) and T_2 (spin-spin) relaxation rates ($1/T_1$ and $1/T_2$, respectively) of the NMR/MRI activatable nanoparticles or the nanosensors in the presence or absence of thrombin were measured and plotted against Gd concentration (for T_1) and against Fe concentration (for T_2) in Fig. S5.† The slope of the relaxation curve indicated relaxivity of the materials. The percentage changes of relaxivities of the nanosensors after the enzymatic cleavage of ThrPep, compared with the ones before enzyme reaction, are presented in Table 1. The non-activatable nanoparticles (control nanosensors: IONC-dThrPep-GdDTPA) were also synthesized using non-cleavable d-ThrPep and were also tested. These were named NS1-C, NS2-

Table 1 Magnetic relaxivity at 9.4 T of the nanosensors (in buffer 50 mM NaHCO₃, pH 8.0, at room temperature) based on the concentration of the contrast materials (sum concentration of Gd and Fe)

Nanosensor	Peptide/nanosensor (nmoles mg ⁻¹)	Gd/Fe molar ratio	Thrombin	r_1 (mM ⁻¹ s ⁻¹)	r_2 (mM ⁻¹ s ⁻¹)	% change r_1	% change r_2
NS1	20	0.0023	–	41.0 ± 0.9	463.3 ± 4.6	109	35
			+	85.7 ± 0.8	625.7 ± 6.7		
NS2	31	0.0030	–	42.3 ± 3.1	479.0 ± 10.5	108	37
			+	87.9 ± 2.8	657.0 ± 27.1		
NS3	48	0.0041	–	42.4 ± 2.6	458.4 ± 14.8	36	31
			+	57.9 ± 1.4	601.7 ± 13.3		
NS4	67	0.0050	–	44.7 ± 0.3	464.5 ± 7.4	21	19
			+	54.1 ± 0.9	551.7 ± 11.4		
NS1-C	21	0.0023	–	41.8 ± 0.8	468.1 ± 4.1	26	23
			+	52.7 ± 1.0	575.4 ± 14.6		
NS2-C	30	0.0029	–	43.9 ± 2.0	471.3 ± 4.6	6	7
			+	46.5 ± 2.1	505.1 ± 1.9		
NS3-C	49	0.0042	–	44.1 ± 0.9	451.1 ± 8.0	2	3
			+	45.2 ± 0.8	466.0 ± 5.6		
NS4-C	65	0.0049	–	44.6 ± 0.2	469.5 ± 7.5	4	2
			+	46.4 ± 0.4	479.8 ± 9.4		

C, NS3-C and NS4-C and had peptide grafting densities similar to their activatable versions (NS1, NS2, NS3 and NS4, respectively).

Table 1 showed that in the absence of thrombin, all the tested nanosensors and control nanosensors had similar T_1 -weighted relaxivity (r_1) values, around 41.0–44.6 mM⁻¹ s⁻¹. In the presence of thrombin, r_1 increased significantly, suggesting the activation of the nanoprobles. The nanosensors with the lower grafting densities (NS1 and NS2 – 0.13 and 0.21 peptide per nm², respectively) showed significantly larger increases in r_1 (109 and 108%), compared to the ones with the higher grafting densities (NS3 and NS4 – 0.32 and 0.44 peptide per nm², 36 and 21%, respectively).

In the absence of thrombin, all the tested nanoparticles exhibited similar T_2 -weighted relaxivity (r_2) values, around 450–489 mM⁻¹ s⁻¹. Interestingly, the percentage change of r_2 was much less than that of r_1 in the presence of thrombin. It indicates that the T_2 effect of the nanosensors was not largely affected upon conjugation with the Gd-DTPA complex. Similar to the change of r_1 , the percentage change of r_2 also decreased from 35% to 19% when the grafting density of ThrPep increased from 20 to 67 nmoles mg⁻¹ nanoparticles. Control nanoparticle or non-activatable nanoprobe with a low peptide density (NS1-C) exhibited some changes in both r_1 and r_2 but the level of change was much less than the change exhibited by NS1, which could be explained by the non-specific cleavage of NS1-C by thrombin. As expected, control nanoparticles with higher grafting densities (NS2-C, NS3-C and NS4-C) did not exhibit pronounced changes in both T_1 and T_2 relaxivities.

These results demonstrated that peptide grafting density had an effect on relaxation behavior of the nanosensors. The higher the density, the smaller the increase in T_1 relaxation rate and the lower the r_1 relaxivity. It was probably because the denser layer of the peptides limited the accessibility of the large enzyme thrombin to the cleavage site, resulting in a lower release of Gd-DTPA and thus a weaker T_1 activation. As

thrombin has molecular weight of 36 kDa and a diameter of around 4 nm, it is reasonable that at higher peptide densities (NS3 and NS4 – 0.32 and 0.44 peptide per nm²), the access of thrombin is hindered.

The data demonstrated the successful synthesis of thrombin-activatable nanosensors. The strong magnetic field induced by the large magnetic moment of the superparamagnetic iron oxide core affected the relaxation process of the much weaker paramagnetic Gd-DTPA, resulting in reduced T_1 signal. Thrombin proteolytically triggered the cleavage of the peptide linker between iron oxide core and Gd-DTPA, resulting in the release of the quenched Gd-DTPA and the subsequent recovery of its T_1 signal in T_1 -weighted MR imaging. Nanosensors with lower peptide grafting density exhibited greater increase in T_1 relaxation rate and would be used for later experiments. Taken together, the developed nanosensor could be of potential use as an activatable NMR/MRI imaging agent for distinguishing fresh and old thrombus, based on the presence or absence of thrombin.

3.3 Dependence of magnetic relaxation activation on thrombin concentration and reaction time

To investigate the effect of thrombin concentration in peptide degradation and the magnetic relaxation activation of the nanosensors, the nanosensor with a lower peptide grafting density (NS1) and the highly grafted nanosensor (NS3) were used. The nanoprobles were exposed to simulated thrombotic conditions (50 × 10⁻³ M NaHCO₃, pH 8) with different thrombin concentrations (0, 0.1, 1, 2 units per mL) for 24 hours at 37 °C. T_1 relaxation was measured on a 400 MHz NMR scanner. Relaxation rates of the samples were plotted against Gd concentration as in Fig. 2A and B. Relaxivities were calculated from the slope of the linear regression generated from the plots and are presented in Fig. 2C.

As the concentration of thrombin increased, T_1 relaxation rate ($1/T_1$) at each nanosensor concentration increased for

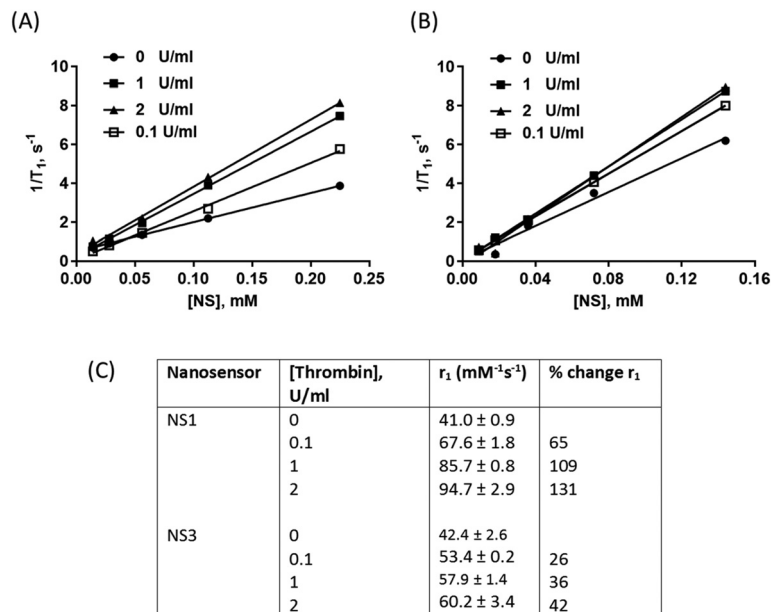
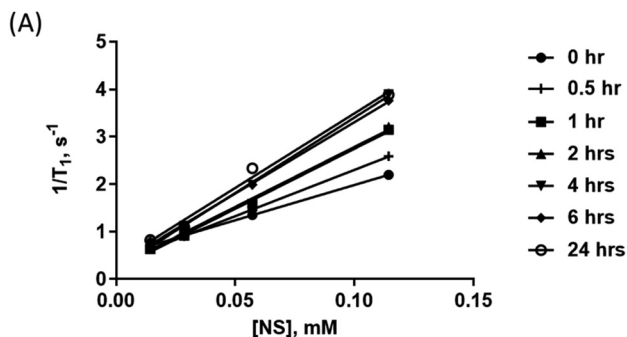


Fig. 2 Effects of thrombin concentrations on magnetic relaxation. (A) and (B) graphs plotting the relationship of relaxation rate and concentration of NS1 and NS3, respectively. (C) Table presenting the effects of thrombin concentrations on magnetic relaxivity of the nanosensors NS1 and NS3. [NS] represents the sum concentration of Gd and Fe in the nanosensor solutions.

both NS1 and NS3. However, the higher thrombin concentration had less impact on the relaxation rate of the NS3 compared to the NS1. Especially there was no change observed in the relaxation rate of NS3 when the enzyme concentration increased from 1 to 2 units per mL. Fig. 3C showed that r_1

relaxivity of NS1 increased by 65%, 109% and 131% while r_1 of NS3 increased by 26%, 36% and 42% as the enzyme concentration increased from 0.1 to 2 $U mL^{-1}$. The concentration-dependent kinetics of relaxivity verified the thrombin-specific activation feature of these nanosensors. These data also confirmed the effect of peptide grafting density on thrombin-induced activation of the synthesized nanoprobes.



(B) Table presenting the effects of reaction time on magnetic relaxivity of the nanosensors NS1 based on Gd concentration. [NS] represents the sum concentration of Gd and Fe in the nanosensor solutions.

Time (hour)	r_1 ($mM^{-1}s^{-1}$)	% change r_1
0	41.0 ± 0.9	
0.5	53.7 ± 0.2	31
1	69.3 ± 1.0	69
2	70.1 ± 1.7	71
4	87.7 ± 0.7	114
6	82.8 ± 3.0	102
24	85.7 ± 1.8	109

Fig. 3 Effects of incubation time on magnetic relaxation. (A) Graph plotting the relationship of relaxation rate and concentration of NS1 at different time points from 0 to 24 hours. (B) Table presenting the effects of reaction time on magnetic relaxivity of the nanosensors NS1 based on Gd concentration. [NS] represents the sum concentration of Gd and Fe in the nanosensor solutions.

The nanosensor NS1 solutions with different concentrations were prepared for the time dependence analysis of thrombin-induced T_1 activation. During the enzymatic process, samples were collected at different time points (0.5, 1, 2, 4, 6, and 24 hours) and then performed T_1 measurement on a 400 MHz NMR scanner. The relaxation rates of the samples were plotted against concentration as shown in Fig. 3A. Relaxivities were calculated from the slope of the linear regression generated from the plots and presented in Fig. 3B. The time-dependent increase of T_1 relaxation rate ($1/T_1$) reflected the relaxivity recovery, corresponding to the release of Gd-DTPA by enzymatic cleavage. The r_1 relaxivity of NS1 increased from 41 ± 0.9 $mM^{-1} s^{-1}$ at 0 h to 87.7 ± 0.7 $mM^{-1} s^{-1}$ at 4 h and then remained at this level at all later time points (6 and 24 h). These data suggested that the enzymatic reaction and the sensing activation of NS1 reached plateau at 4 h, therefore further experiments would be performed with 4 h thrombin incubation.

3.4 MRI-based T_1 -weighted activation of the nanosensor phantoms

Next, we investigated whether the observed thrombin-activated increase in r_1 of the nanosensor results in the increases in the T_1 -weighted signal by MRI or the increase in the brightness of the MR image. In this experiment, we imaged the phantom

solutions of the nanosensors with different peptide grafting densities (NS1, NS2, NS3) and their control non-activatable counterparts (NS1-C, NS2-C, NS3-C). T_1 - and T_2 -weighted MR images of the nanoprobe solutions were acquired before and after 4 h incubation with thrombin.

Large increases in the T_1 -weighted MR signals were observed for NS and NS2 after enzyme reaction (signals increased by approximately 187% and 165%, respectively in Fig. 4A and C). However, the increase in the signal of NS3 (34%) was much lower than those from NS1 and NS2. This again confirmed the hindrance effect of the denser peptide grafting on thrombin accessibility to the cleavage site and thus the lower MRI activation. The control non-activatable counterparts (NS2-C and NS3-C) did not exhibit pronounced increases in T_1 -weighted signals (signals increased by approximately 6% and 8% in Fig. 4A and C) while NS1-C showed an increase in signal (41%). Overall, the increases in T_1 signals from the nanosensors were much greater than the signal increases from their control counterparts. As expected, minimal changes in T_2 -weighted signals were observed from both the nanosensors and their control counterparts due to the absence of T_2 quenching and activation (Fig. 4B and D). Taken together, the above results confirm that our activatable nanoprobe gets activated in the presence of thrombin and the activation was demonstrated by the increase in the T_1 -weighted MRI signal.

3.5 Detecting and discriminating *in vitro* thrombus using the nanosensor

Next, we studied the specific binding of our nanosensor to thrombus and investigated its sensing capability on fresh and

old thrombi. We labelled our nanosensor NS1 with a peptide (FibPep: GPRPPGGS[Lys(TMR)]GC) that was able to specifically bind to fibrin. Fibrin is only present in thrombi and not in circulating blood. Fibrin is found in all thrombi – venous and arterial, fresh and aged thrombi – in high concentration (more than 30 μM).^{39–41} Therefore, fibrin targeting provides high specificity and high sensitivity for imaging both forming and constituted thrombi. Fibrin has been employed as a target for development of MR imaging probes based on Gd-DTPA (EP-1873)⁴² and Gd-DOTA (EP-2104R);²³ imaging nanoparticles based on iron oxide;^{29–32} and manganese oxide or manganese oleate.^{35,43}

In vitro human thrombi were prepared using fresh frozen plasma (FFP) in 0.6 mL eppendorf tubes and incubated with NS1 at different concentrations ranging from 0 to 2 mg mL^{-1} . Agarose gel was added on top of the thrombus for MR imaging. Fig. 5B presents MR images of the thrombi. For each concentration group, the left image is the T_1 -weighted image and the right one is the T_2 -weighted image. It was clear that in the T_1 -weighted imaging, the thrombi incubated with NS1 exhibited bright signal along the top surface of the thrombi while the same phenomenon was not observed for the control thrombus (the thrombus without the nanoparticles). As the concentration of NS1 increased from 0.5 to 1.0 mg mL^{-1} , the T_1 signal also increased (Fig. 5D). However, the signal decreased significantly once the NS1 concentration reached 2 mg mL^{-1} . This was probably due to the high density of the NS1 binding on the thrombus surface, which hindered the access of thrombin to the cleavage site. Therefore, a majority of NS1 nanoparticles was intact and not activated to show a

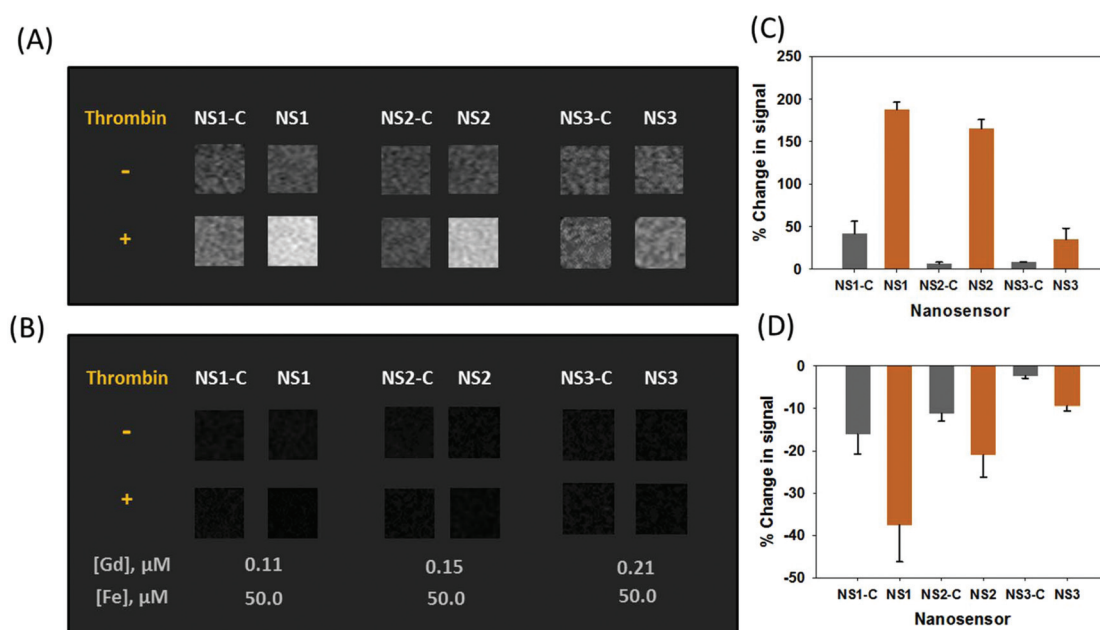


Fig. 4 Magnetic resonance imaging (MRI) of activatable and non-activatable nanosensors in the presence and absence of thrombin enzyme. (A) T_1 -Weighted images and (B) T_2 -weighted images of the nanosensor phantoms. (C) and (D) graphs presenting changes in T_1 - and T_2 -signal of the nanoparticles after incubation with thrombin, respectively.

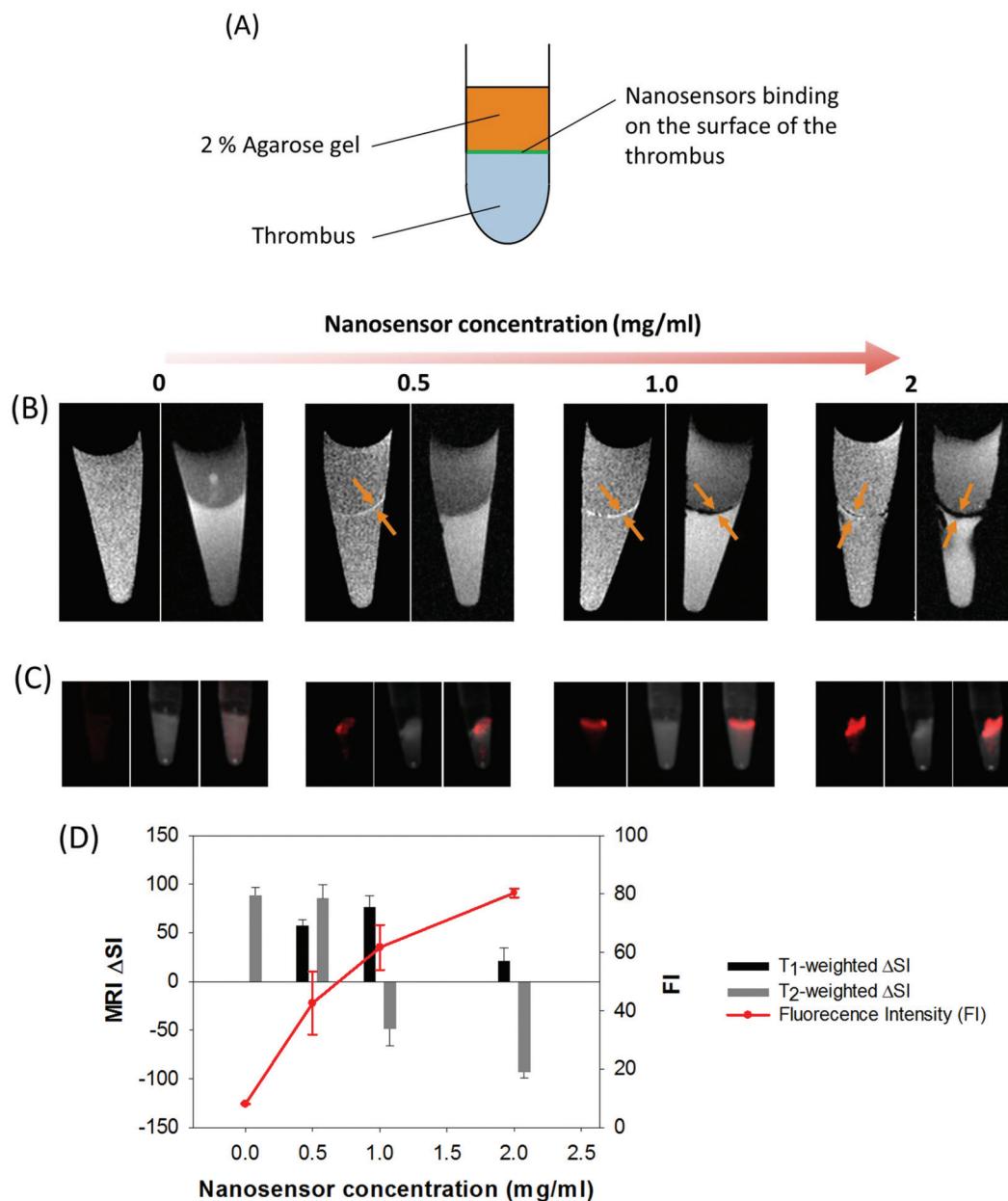


Fig. 5 *In vitro* human thrombus binding assay with different concentrations of the nanosensors. (A) Illustration of the 0.6 mL tube containing the thrombus in this experiment. (B) MR images of thrombi incubated with NS1 at different concentrations under a 9.4 T MRI. For each concentration, the left image is T_1 -weighted image and the right one is T_2 -weighted. The top edge of the thrombi appears bright (signal enhancement) in T_1 -weighted images and appears dark (signal diminishment) at high concentrations of the nanosensors in T_2 -weighted images. Orange arrows point to the surface of the thrombus where the nanosensors attached and enhanced or diminished the signal. (C) Fluorescence, reflectance and merged images of the thrombi recorded with a Carestream FX-Pro. (D) Graph plotting T_1 - and T_2 -weighted signal intensity (ΔSI) and fluorescence intensity of thrombus edge. ΔSI was calculated as signal difference of thrombus edge and the agarose gel on top of the thrombus.

strong T_1 signal. In fact, when the concentration of NS1 increased to 1.0 and 2 mg mL⁻¹, we observed a decrease in T_2 -weighted signal (Fig. 5D). It could also be explained by the binding of a large number of NS1 of which a majority was still intact or not activated. Fig. 5C shows the fluorescence images of the thrombi incubated with NS1 at different concentrations. The higher the concentration of NS1, the stronger the fluo-

rescence signal intensity (Fig. 5D), confirming the higher number of NS1 binding on the surface of the thrombi.

Next, we synthesized different nanosensors and control nanosensors. TF or IONC-ThrPep-GdDTPA-FibPep was prepared using cleavable ThrPep and fibrin-targeting FibPep. T_{CF} or IONC-dThrPep-GdDTPA-FibPep was synthesized using non-cleavable dThrPep and fibrin-targeting FibPep. T_{FC} or

IONC-ThrPep-GdDTPA-ConFibPep was prepared using cleavable ThrPep and non-fibrin-binding ConFibPep peptides. $T_C F_C$ or IONC-dThrPep-GdDTPA-ConFibPep was synthesized using non-cleavable dThrPep and non-binding ConFibPep peptides. These nanoparticles were synthesized and controlled to have the same iron and gadolinium content, approximately 50 and 0.11 μM respectively. They showed the zeta potential of around -29 and the hydrodynamic size of around 170 nm. Both fresh (12 hour) and old (7 day) human thrombi were prepared and incubated with these nanoparticles at a concentration of 1.5 mg mL^{-1} .

Fig. 6A shows MR images of the thrombi. For each group of images, the left image is the T_1 -weighted image and the right one is the T_2 -weighted image. The fresh thrombus incubated with TF nanosensor exhibited both T_1 -signal (bright) and T_2 -

signal (dark). The presence of both T_1 and T_2 effect was due to the high concentration of the TF as explained above. The old thrombus incubated with TF, on the other hand, did not show T_1 -signal but exhibited T_2 -signal. Both fresh and aged thrombi that were incubated with $T_C F$ showed no T_1 - but T_2 -signal as $T_C F$ were non-cleavable and not activated in T_1 -weighted imaging. All fresh and aged thrombi incubated with $T_F C$ or $T_C F_C$ showed neither T_1 - nor T_2 -signal as there was no particles binding on these thrombi. This was because $T_F C$ and $T_C F_C$ were non-binding nanoparticles as they were prepared with a peptide that did not bind to fibrin. This was confirmed by the fluorescence images of the thrombi shown in Fig. 6B. Fresh and aged thrombi incubated with TF and $T_C F$ exhibited strong fluorescence while those incubated with $T_F C$ and $T_C F_C$ showed no fluorescence. These images proved the binding of TF and

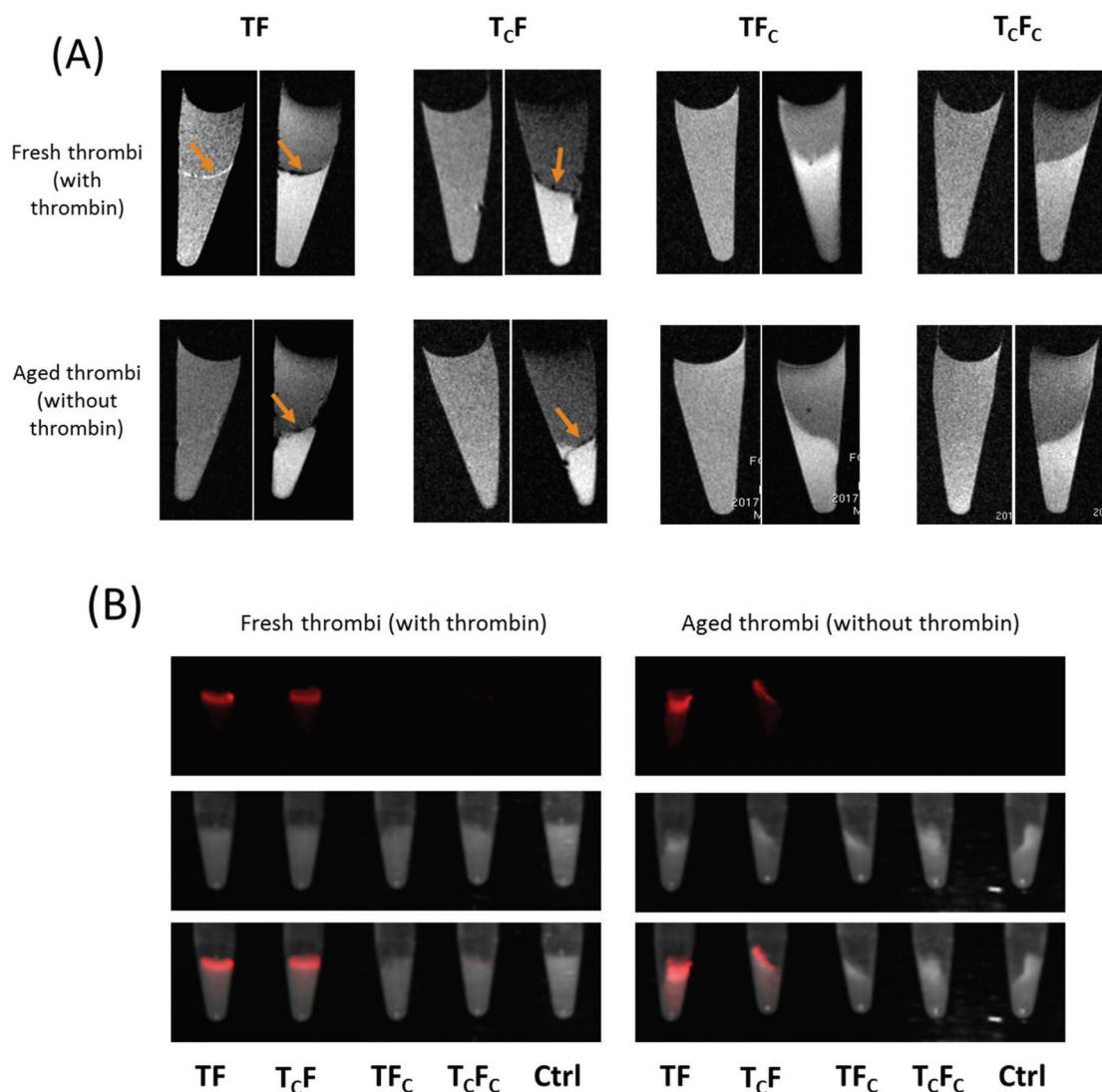


Fig. 6 *In vitro* human thrombus binding assay with different nanoparticles. TF is a targeting and cleavable nanosensor. $T_C F$ is a targeting and non-cleavable nanoparticle. $T_F C$ is a non-targeting but cleavable nanosensor. $T_C F_C$ is a non-targeting and non-cleavable nanoparticle. (A) MR images of thrombi incubated with different nanoparticles. For each nanoparticle, the left image is T_1 -weighted image and the right one is T_2 -weighted. (B) Fluorescence images (top row), reflectance images (middle row), and merged images (bottom row) of the thrombi.

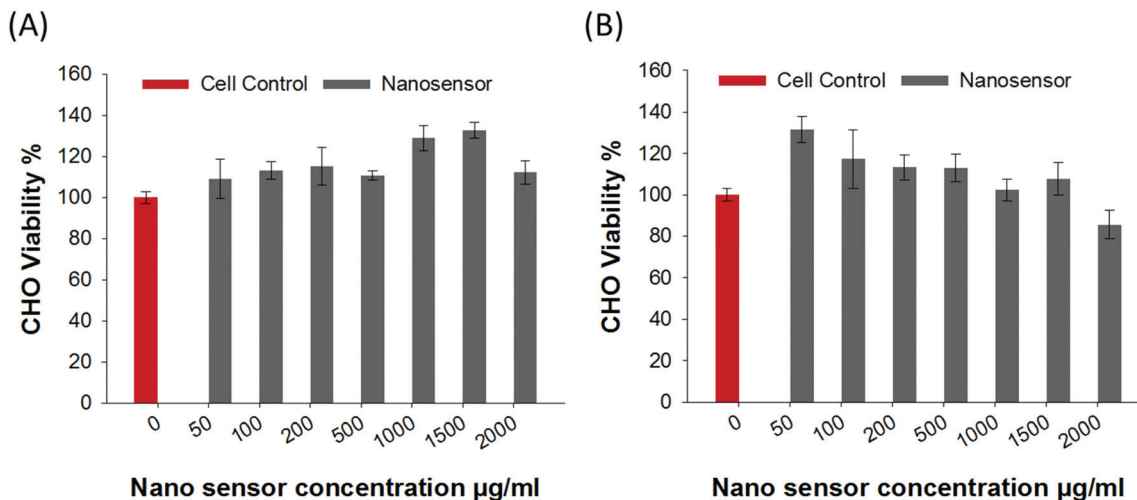


Fig. 7 Cytotoxicity study. Graphs illustrating cell viability after incubated with the nanosensors for 1 day (A) and 2 days (B).

T_CF nanoparticles to the thrombi and the non-binding of T_CF_C and T_CF_C particles. The presented data proved that the developed nanosensor TF was able to bind specifically to thrombus *via* fibrin targeting peptide and that TF was able to switch between *T*₁ and *T*₂ MR signals based on the presence or absence of thrombin.

3.6 *In vitro* biocompatibility of the nanosensor

Chinese Hamster Ovarian (CHO) cells were incubated with nanosensor NS1 at different concentrations ranging from 0 to 2 mg mL⁻¹ for 1 day and 2 days (Fig. 7). PrestoBlue Cell Viability Reagent was used to assess cell viability. When added to cells, the PrestoBlue reagent is modified by the reducing environment of the viable cell and turns red in colour, becoming highly fluorescent. This colour change can be detected using fluorescence measurements. In our study, the cells showed good viability at all tested concentrations of NS1 after 1 day. A slight reduction of cell viability was observed on cells incubated with NS1 at very high concentration (2 mg mL⁻¹) at day 2. Despite the reduction, cell viability was still over 80% and the difference was not significant ($p = 0.1373$, compared with control cells). These data suggested the good cell biocompatibility of the developed nanosensor.

Current diagnostic techniques are clearly of a high standard but further improvements are required, therefore several groups are working on different approaches for molecular imaging. Great attention is being directed to the development of activatable “smart” nanosensors. Activatable sensors can solve the problem of a high-signal-to-noise ratio, and reduce the risk of false-positive results. “Smart” nanosensors only become activated in the presence of their target and have at least one property operating at the nanoscale. Probes in this size range often show a high penetration efficiency,⁴⁴ are generally biocompatible,⁴⁵ and might increase the circulation time of the probe, because nanomaterials are often more stable than chemical probes.⁴⁴

Most of these smart activatable nanosensors are targeting cancer-specific properties. However Chen *et al.*,⁴⁶ Nahrendorf *et al.*⁴⁷ and Medintz *et al.*⁴⁸ proposed smart nanosensors for monitoring the activity of proteases that are associated with atherosclerotic lesions. These sensors consisted of a Fluorescence Resonance Energy Transfer (FRET) pair that was connected *via* a protease cleavable peptide. In presence of the respective protease, *e.g.* thrombin or cathepsin B, the sensors became activated.⁴⁸ However the fluorescence value depended on intensity of incident light, depth and size of lesion, making an additional reference probe necessary.^{49,50} With the intention of avoiding an additional reference probe, nanosensors designed for MRI imaging could be a promising alternative for thrombus detection. This has led us to the development of the smart nanosensors for thrombus detection and also for differentiation between old and new thrombi in this study. Our work has a great potential to take cardiovascular disease imaging to the next level with great benefit to patients. Mouse models of fresh and old thrombi are currently under development and the MRI *T*₁/*T*₂ signal switchability of these nanosensors will be tested in a near future.

4. Conclusion

The presented data demonstrate the successful synthesis of a novel activatable nanosensor for detecting and aging thrombus. Iron oxide nanoclusters (IONCs) were functionalized with Gd-DTPA (diethylenetriamine penta-acetic acid gadolinium(III) dihydrogensalhydrate) over a thrombin cleavable peptide. Gd-DTPA was further labelled with a dye containing fibrin-binding peptide for targeting both fresh and old thrombi. While the IONCs exhibit a *T*₂ (spin-spin relaxation) enhancing effect, Gd-DTPA strengthens the *T*₁ (spin-lattice relaxation) contrast in MRI. However the *T*₁ effect through Gd-DTPA was quenched in close proximity to IONC and could be restored by separating the two contrast agents. Thrombin is present on fresh throm-

bus, thus a separation of Gd-DTPA and IONC can occur in the presence of new thrombi. We have successfully demonstrated the thrombin-induced activation of our nanosensor *via* both NMR and MRI. The activation was depended on the grafting density of the thrombin-cleavable peptide that connected IONC core with Gd-DTPA. The higher the density, the lower the activation. Using human thrombi, we successfully demonstrated that these novel nanosensors were able to distinguish between fresh and aged thrombi *in vitro*. The nanosensor appeared to be non-toxic to the cells within the tested concentrations.

The nanosensors developed and characterized in this study provide products with great potential for translation to a clinical diagnostic role in identifying fresh thrombus which is most susceptible to the fibrinolytic action of enzymes aimed at restoring cardiac or cerebral blood flow. The nanoprobe, thus, have great potential in reducing morbidity and mortality in such vulnerable patients. The working principle demonstrated in this study can be applied to many other diseases such as cancer.

Conflicts of interest

There are no conflicts to declare.

Acknowledgements

This work received financial support from the Australian National Health and Medical research council (H. T. T.: APP1037310, APP1159899) and Australian research council (A. K. W.: CE140100036). The authors would like to acknowledge the Australian National Fabrication Facility (Queensland Node); National Imaging Facility, Centre for Advanced Imaging for access to key items of equipment.

References

- X. Wang and K. Peter, *Arterioscler., Thromb., Vasc. Biol.*, 2017, **37**, 1029.
- J. R. McCarthy, *Curr. Cardiovasc. Imaging Rep.*, 2010, **3**, 42–49.
- E. J. Benjamin, M. J. Blaha, S. E. Chiuvé, M. Cushman, S. R. Das, R. Deo, S. D. de Ferranti, J. Floyd, M. Fornage, C. Gillespie, C. R. Isasi, M. C. Jiménez, L. C. Jordan, S. E. Judd, D. Lackland, J. H. Lichtman, L. Lisabeth, S. Liu, C. T. Longenecker, R. H. Mackey, K. Matsushita, D. Mozaffarian, M. E. Mussolino, K. Nasir, R. W. Neumar, L. Palaniappan, D. K. Pandey, R. R. Thiagarajan, M. J. Reeves, M. Ritchey, C. J. Rodriguez, G. A. Roth, W. D. Rosamond, C. S. S. Sasson, A. Towfighi, C. W. Tsao, M. B. Turner, S. S. Virani, J. H. Voeks, J. Z. Willey, J. T. Wilkins, J. H. Y. Wu, H. M. Alger, S. S. Wong and P. Muntner, *Circulation*, 2017, **135**, e146–e603.
- D. Mozaffarian, E. J. Benjamin, A. S. Go, D. K. Arnett, M. J. Blaha, M. Cushman, S. de Ferranti, J. P. Despres, H. J. Fullerton, V. J. Howard, M. D. Huffman, S. E. Judd, B. M. Kissela, D. T. Lackland, J. H. Lichtman, L. D. Lisabeth, S. Liu, R. H. Mackey, D. B. Matchar, D. K. McGuire, E. R. Mohler 3rd, C. S. Moy, P. Muntner, M. E. Mussolino, K. Nasir, R. W. Neumar, G. Nichol, L. Palaniappan, D. K. Pandey, M. J. Reeves, C. J. Rodriguez, P. D. Sorlie, J. Stein, A. Towfighi, T. N. Turan, S. S. Virani, J. Z. Willey, D. Woo, R. W. Yeh, M. B. Turner, C. American Heart Association Statistics and S. Stroke Statistics, *Circulation*, 2015, **131**, e29–322.
- S. P. Jackson, W. S. Nesbitt and E. Westein, *J. Thromb. Haemostasis*, 2009, **7**(Suppl. 1), 17–20.
- M. B. Srichai, C. Junor, L. L. Rodriguez, A. E. Stillman, R. A. Grimm, M. L. Lieber, J. A. Weaver, N. G. Smedira and R. D. White, *Am. Heart J.*, 2006, **152**, 75–84.
- F. Pomero, F. Dentali, V. Borretta, M. Bonzini, R. Melchio, J. D. Douketis and L. M. Fenoglio, *Thromb. Haemostasis*, 2013, **109**, 137–145.
- K. L. Ciesinski and P. Caravan, *Curr. Cardiovasc. Imaging Rep.*, 2010, **4**, 77–84.
- P. F. Fedullo and V. F. Tapson, *N. Engl. J. Med.*, 2003, **349**, 1247–1256.
- T. Moulin, F. Cattin, T. Crepin-Leblond, L. Tatu, D. Chavot, M. Piotin, J. F. Viel, L. Rumbach and J. F. Bonneville, *Neurology*, 1996, **47**, 366–375.
- F. Blasi, B. L. Oliveira, T. A. Rietz, N. J. Rotile, P. C. Naha, D. P. Cormode, D. Izquierdo-Garcia, C. Catana and P. Caravan, *Arterioscler., Thromb., Vasc. Biol.*, 2015, **35**, 2114–2121.
- D. B. Buxton, M. Antman, N. Danthi, V. Dilsizian, Z. A. Fayad, M. J. Garcia, M. R. Jaff, M. Klimas, P. Libby, M. Nahrendorf, A. J. Sinusas, S. A. Wickline, J. C. Wu, R. O. Bonow and R. Weissleder, *Circulation*, 2011, **123**, 2157–2163.
- J. R. Lindner, *Circulation*, 2012, **125**, 3057–3059.
- H. T. Ta, Z. Li, C. E. Hagemeyer, G. Cowin, S. Zhang, J. Palasubramaniam, K. Alt, X. Wang, K. Peter and A. K. Whittaker, *Biomaterials*, 2017, **134**, 31–42.
- Z. Li, P. W. Yi, Q. Su, H. Lei, H. L. Zhao and Z. H. Zhu, *Adv. Funct. Mater.*, 2012, **22**, 2387–2393.
- H. T. Ta, S. Prabhu, E. Leitner, F. Jia, D. von Elverfeldt, K. E. Jackson, T. Heidt, A. K. Nair, H. Pearce, C. von Zur Muhlen, X. Wang, K. Peter and C. E. Hagemeyer, *Circ. Res.*, 2011, **109**, 365–373.
- C. E. Hagemeyer, K. Alt, A. P. Johnston, G. K. Such, H. T. Ta, M. K. Leung, S. Prabhu, X. Wang, F. Caruso and K. Peter, *Nat. Protoc.*, 2015, **10**, 90–105.
- H. T. Ta, K. Peter and C. E. Hagemeyer, *Trends Cardiovasc. Med.*, 2012, **22**, 105–111.
- H. T. Ta, Z. Li, C. E. Hagemeyer, G. Cowin, J. Palasubramaniam, K. Peter and A. K. Whittaker, *Atherosclerosis*, 2017, **263**, e146.
- H. T. Ta, S. Prabhu, E. Leitner, F. Jia, K. Putnam, N. Bassler, K. Peter and C. E. Hagemeyer, *Atherosclerosis*, 2015, **241**, e26.

- 21 H. T. Ta, Z. Li, Y. Wu, G. Cowin, S. Zhang, A. Yago, A. K. Whittaker and Z. P. Xu, *Mater. Res. Express*, 2017, **4**, 116105.
- 22 A. Phinikaridou, M. E. Andia, S. Lacerda, S. Lorrio, M. R. Makowski and R. M. Botnar, *Molecules*, 2013, **18**, 14042–14069.
- 23 K. Overoye-Chan, S. Koerner, R. J. Looby, A. F. Kolodziej, S. G. Zech, Q. Deng, J. M. Chasse, T. J. McMurphy and P. Caravan, *J. Am. Chem. Soc.*, 2008, **130**, 6025–6039.
- 24 J. Vymazal, E. Spuentrup, G. Cardenas-Molina, A. J. Wiethoff, M. G. Hartmann, P. Caravan and E. C. Parsons Jr., *Invest. Radiol.*, 2009, **44**, 697–704.
- 25 D. Collen and H. R. Lijnen, *Thromb. Haemost.*, 2005, **93**, 627–630.
- 26 J. S. Balami, R. Chen, B. A. Sutherland and A. M. Buchan, *CNS Neurol. Disord.: Drug Targets*, 2013, **12**, 145–154.
- 27 W. Theiss, A. Wirtzfeld, U. Fink and P. Maubach, *Angiology*, 1983, **34**, 61–69.
- 28 M. Niemann, P. D. Gaudron, B. Bijmens, S. Störk, M. Beer, H. Hillenbrand, M. Cikes, S. Herrmann, K. Hu, G. Ertl and F. Weidemann, *Circ. Cardiovasc. Imag.*, 2012, **5**, 667–675.
- 29 J. R. McCarthy, P. Patel, I. Botnaru, P. Haghayeghi, R. Weissleder and F. A. Jaffer, *Bioconjugate Chem.*, 2009, **20**, 1251–1255.
- 30 A. M. Wen, Y. Wang, K. Jiang, G. C. Hsu, H. Gao, K. L. Lee, A. C. Yang, X. Yu, D. I. Simon and N. F. Steinmetz, *J. Mater. Chem. B*, 2015, **3**, 6037–6045.
- 31 L. W. Starmans, R. P. Moonen, E. Aussems-Custers, M. J. Daemen, G. J. Strijkers, K. Nicolay and H. Grull, *PLoS One*, 2015, **10**, e0119257.
- 32 L. W. Starmans, D. Burdinski, N. P. Haex, R. P. Moonen, G. J. Strijkers, K. Nicolay and H. Grull, *PLoS One*, 2013, **8**, e57335.
- 33 M. V. Yigit, D. Mazumdar and Y. Lu, *Bioconjugate Chem.*, 2008, **19**, 412–417.
- 34 J. S. Choi, J. H. Lee, T. H. Shin, H. T. Song, E. Y. Kim and J. Cheon, *J. Am. Chem. Soc.*, 2010, **132**, 11015–11017.
- 35 D. Pan, A. Senpan, S. D. Caruthers, T. A. Williams, M. J. Scott, P. J. Gaffney, S. A. Wickline and G. M. Lanza, *Chem. Commun.*, 2009, 3234–3236, DOI: 10.1039/b902875g.
- 36 S. Santra, S. D. Jativa, C. Kaittanis, G. Normand, J. Grimm and J. M. Perez, *ACS Nano*, 2012, **6**, 7281–7294.
- 37 S. T. Gunawan, K. Kempe, T. Bonnard, J. Cui, K. Alt, L. S. Law, X. Wang, E. Westein, G. K. Such, K. Peter, C. E. Hagemeyer and F. Caruso, *Adv. Mater.*, 2015, **27**, 5153–5157.
- 38 D. S. Waugh, *Protein Expression Purif.*, 2011, **80**, 283–293.
- 39 V. J. Marder, D. J. Chute, S. Starkman, A. M. Abolian, C. Kidwell, D. Liebeskind, B. Ovbiagele, F. Vinuela, G. Duckwiler, R. Jahan, P. M. Vespa, S. Selco, V. Rajajee, D. Kim, N. Sanossian and J. L. Saver, *Stroke*, 2006, **37**, 2086–2093.
- 40 E. Spuentrup, B. Fausten, S. Kinzel, A. J. Wiethoff, R. M. Botnar, P. B. Graham, S. Haller, M. Katoh, E. C. Parsons Jr., W. J. Manning, T. Busch, R. W. Gunther and A. Buecker, *Circulation*, 2005, **112**, 396–399.
- 41 E. Spuentrup, M. Katoh, A. Buecker, B. Fausten, A. J. Wiethoff, J. E. Wildberger, P. Haage, E. C. J. Parsons, R. M. Botnar, P. B. Graham, M. Vettelschoss and R. W. Günther, *Invest. Radiol.*, 2007, **42**, 586–595.
- 42 R. M. Botnar, A. S. Perez, S. Witte, A. J. Wiethoff, J. Laredo, J. Hamilton, W. Quist, E. C. J. Parsons, A. Vaidya, A. Kolodziej, J. A. Barrett, P. B. Graham, R. M. Weisskoff, W. J. Manning and M. T. Johnstone, *Circulation*, 2004, **109**, 2023–2029.
- 43 D. Pan, S. D. Caruthers, G. Hu, A. Senpan, M. J. Scott, P. Gaffney, S. A. Wickline and G. M. Lanza, *J. Am. Chem. Soc.*, 2008, **130**, 9186–9187.
- 44 S. Deb, K. Ghosh and S. D. Shetty, *Indian J. Med. Res.*, 2015, **141**, 285–298.
- 45 H. Arami, A. Khandhar, D. Liggitt and K. M. Krishnan, *Chem. Soc. Rev.*, 2015, **44**, 8576–8607.
- 46 J. Chen, C.-H. Tung, U. Mahmood, V. Ntziachristos, R. Gyurko, M. C. Fishman, P. L. Huang and R. Weissleder, *Circulation*, 2002, **105**, 2766.
- 47 M. Nahrendorf, P. Waterman, G. Thurber, K. Groves, M. Rajopadhye, P. Panizzi, B. Marinelli, E. Aikawa, M. J. Pittet, F. K. Swirski and R. Weissleder, *Arterioscler., Thromb., Vasc. Biol.*, 2009, **29**, 1444–1451.
- 48 I. L. Medintz, A. R. Clapp, F. M. Brunel, T. Tiefenbrunn, H. Tetsuo Uyeda, E. L. Chang, J. R. Deschamps, P. E. Dawson and H. Mattoussi, *Nat. Mater.*, 2006, **5**, 581–589.
- 49 K. Welsler, R. Adsley, B. M. Moore, W. C. Chan and J. W. Aylott, *Analyst*, 2011, **136**, 29–41.
- 50 M. F. Kircher, R. Weissleder and L. Josephson, *Bioconjugate Chem.*, 2004, **15**, 242–248.

SUPPORTING INFORMATION to

Activatable Magnetic Resonance Nanosensor as a Potential Imaging Agent for Detecting and Discriminating Thrombosis

Supplementary Figures

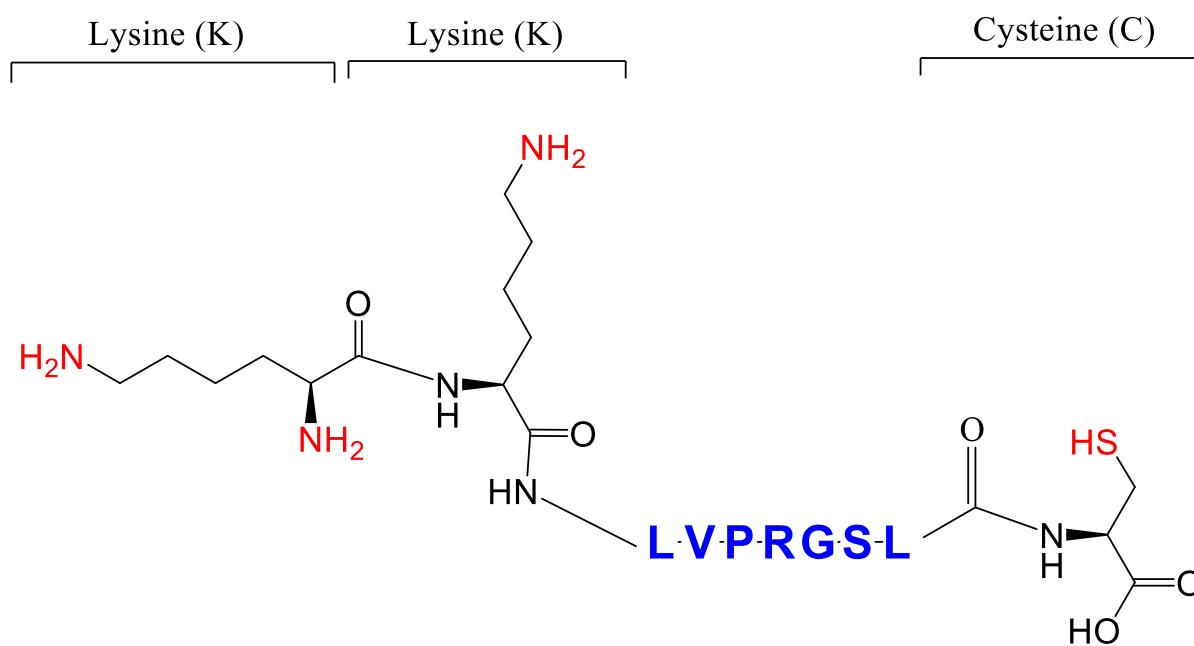


Figure S1: Thrombin-cleavable peptide (ThrPep) – KKL \cdot VPRGSLC

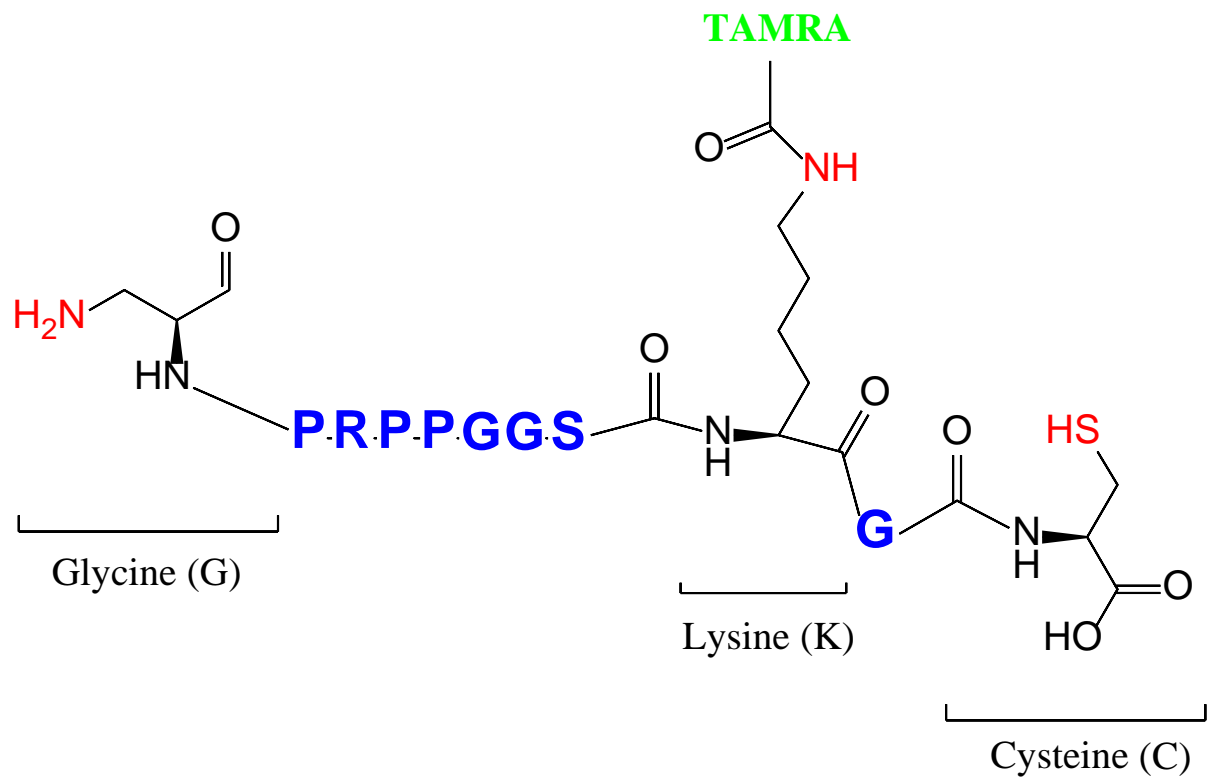


Figure S2: Fibrin binding peptide (FibPep): GPRPPGGS{Lys(TMR)}GC.

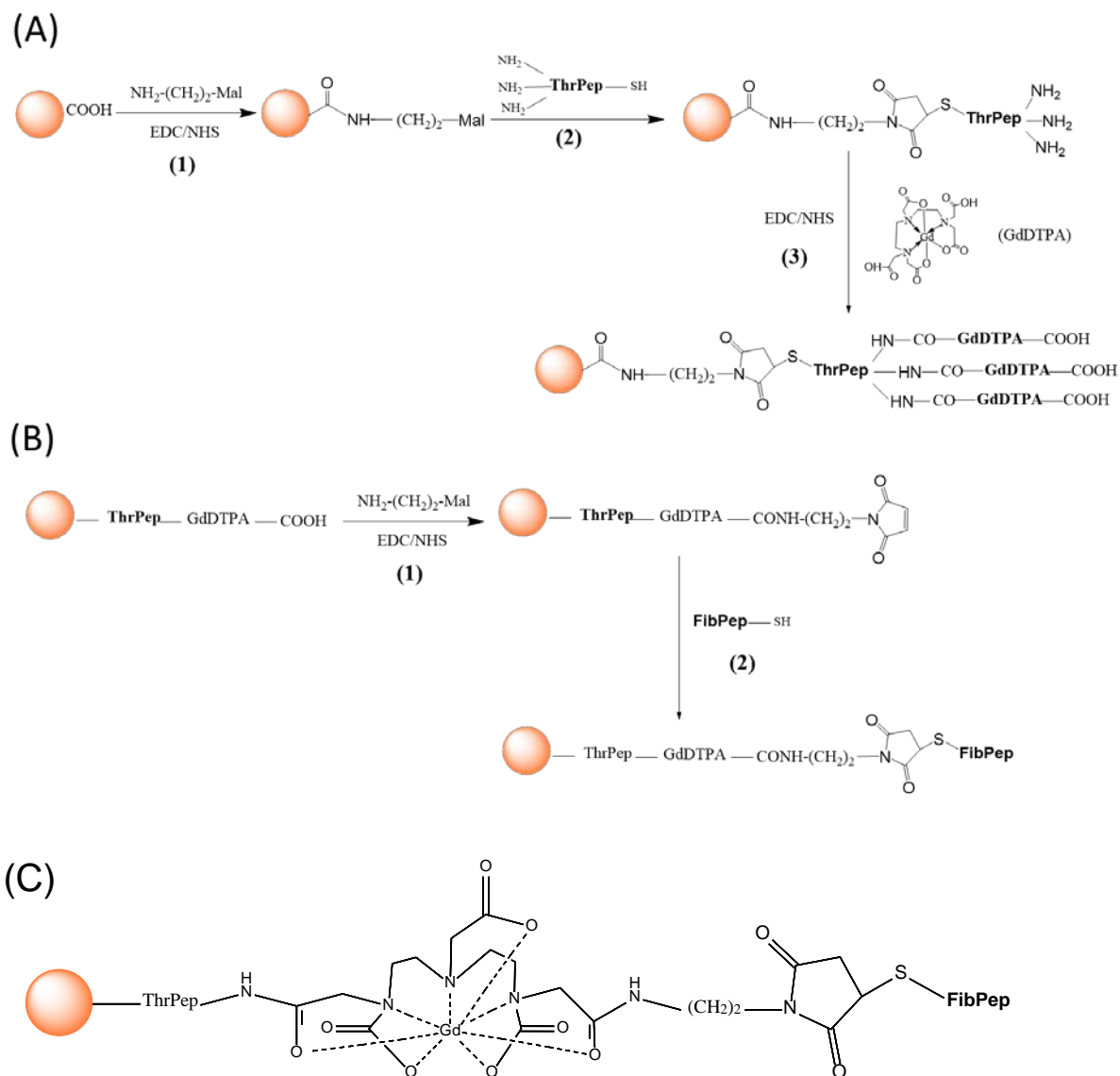


Figure S3: Image illustrating the synthesis of the nanosensor. **(A)** Conjugation steps to prepare the nanosensor. The protocol including (1) the introduction of maleimide functional group to IONC surface via carbodiimide reaction, carboxyl activation using EDC and NHS; (2) the attachment of ThrPep to IONC surface via maleimide-thiol reaction; and (3) the introduction of Gd-DTPA layer via carbodiimide reaction. Each ThrPep was loaded with a maximum of three Gd-DTPA. **(B)** Conjugation steps to label the nanosensor with the binding peptide FibPep. The protocol including (1) the introduction of maleimide functional group to nanosensor surface via carbodiimide reaction, carboxyl activation using EDC and NHS; and (2) the attachment of

FibPep to the nanosensor via maleimide-thiol reaction. (C) Chemical structure of the nanosensor. ThrPep: thrombin-cleavable peptide. FibPep: fibrin-binding peptide.

(A)

Hydrodynamic size and zeta potential of nanoparticles			
Sample	Z-average	PDI	Zeta potential
Bare iron oxide nanocluster (IONC)	103.2 ± 2.1	0.255 ± 0.016	-44.5 ± 1.4
IONC-ThrPep-GdDTPA	134.1 ± 1.5	0.314 ± 0.034	-36.7 ± 0.9
IONC-ThrPep-GdDTPA-FibPep	170.0 ± 1.9	0.269 ± 0.006	-29.1 ± 0.7

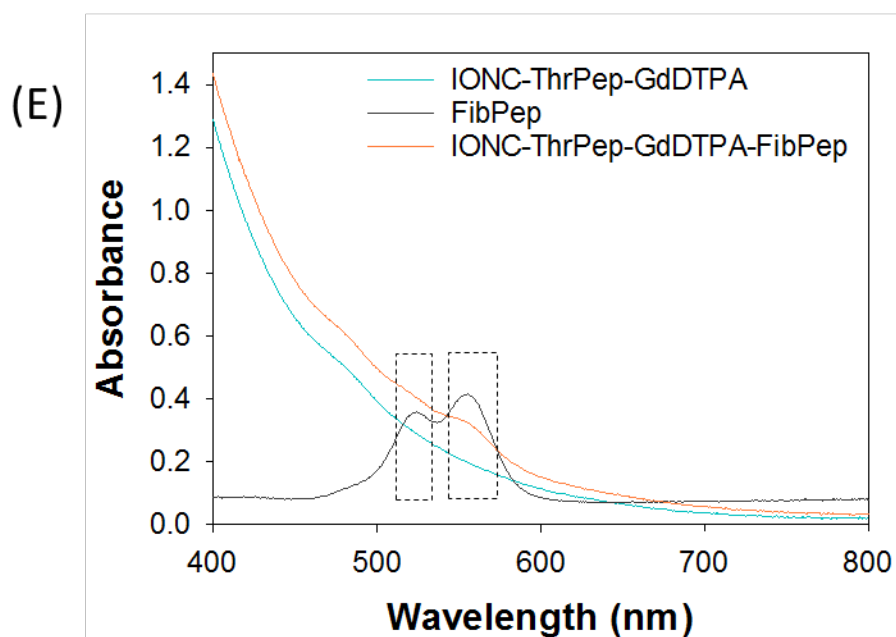
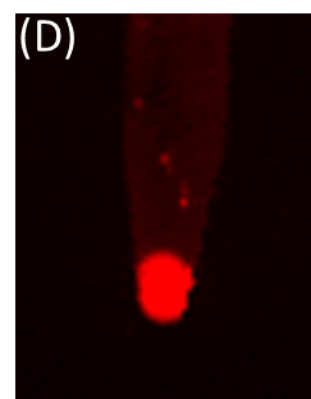
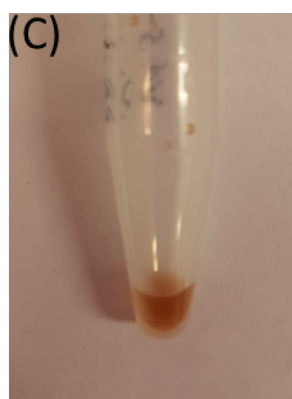
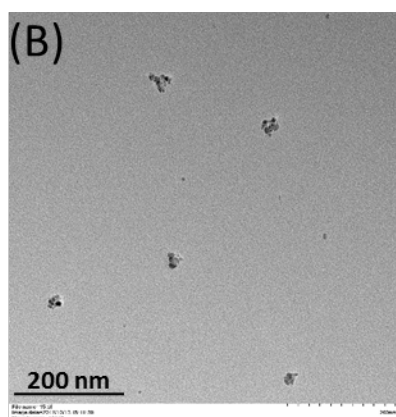


Figure S4: Characteristics of the nanosensors. (A) Hydrodynamic size and zeta potential of the nanoparticles. (B) TEM image of the FibPep-nanosensor. (C) Color image of the FibPep-nanosensor. (D) Fluorescence image of the FibPep-nanosensor. (E) UV-Vis Spectra.

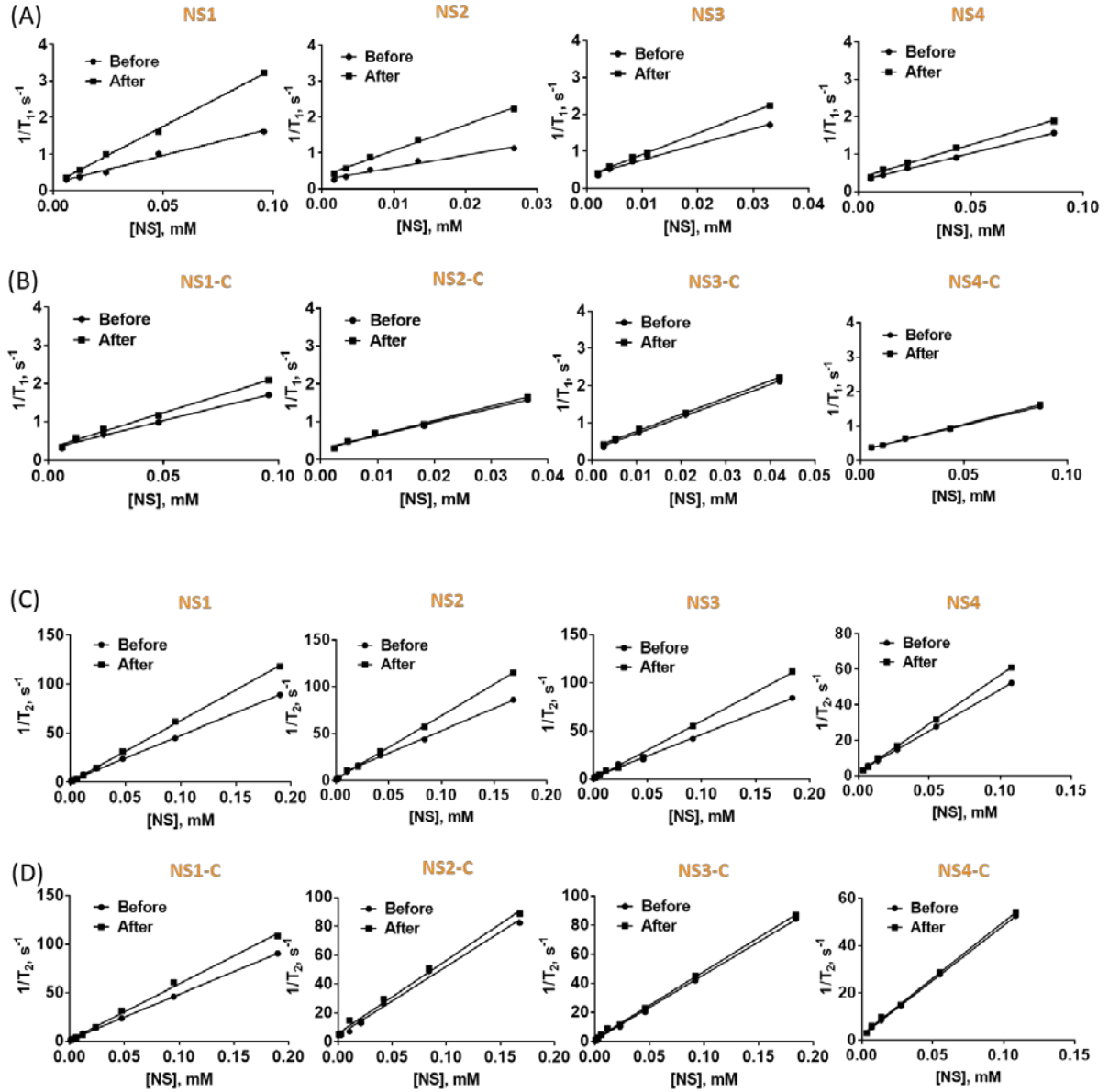


Figure S5: Relaxation of the nanosensors (NS) and control non-activatable nanosensor (NS-C) prepared with different grafting density of ThrPep. (A) T_1 relaxation of activatable nanoparticles (nanosensors). (B) T_1 relaxation of non-activatable nanoparticles (control nanosensors). (C) T_2 relaxation of activatable nanoparticles (nanosensors). (D) T_2 relaxation of non-activatable nanoparticles (control nanosensors). $[NS]$ represents the sum concentration of Gd and Fe in the nanosensor solutions.